Electronic Supplementary Material (ESI) for Journal of Materials Chemistry A.
This journal is © The Royal Society of Chemistry 2018

ELECTRONIC SUPPLEMENTARY INFORMATION

High-efficiency organic solar cells based on a haloid salt and polyfluorene polymer with high alignment-level of cathode selective contact

Victor S. Balderrama*[a], José G. Sánchez[b], Gonzalo Lastra[c], Werther Cambarau[d], Saúl Arias[e], Josep Pallarès[b], Emilio Palomares*[d], Magali Estrada[e] and Lluis F. Marsal*[b]

[a]*CONACYT - Center for Engineering and Industrial Development, CIDESI, Micro-Electro-Mechanical Systems Department (MEMS), 76125 Santiago de Querétaro, Querétaro, Mexico. E-mail: vbalderrama@conacyt.mx; victor.balderrama@cidesi.edu.mx*

[b]*Department of Electric, Electronic and Automatic Control, Universitat Rovira i Virgili, 43007, Tarragona, Spain. E-mail: lluis.marsal@urv.cat*

[c]*UPIITA, Instituto Politécnico Nacional, 07340, Mexico City, México*

[d]*Institute of Chemical Research of Catalonia (ICIQ-BIST), 43007 Tarragona, Spain. Email: epalomares@iciq.es*

[e]*Solid State Electronics Section, Department of Electrical Engineering, Center for Research and Advanced Studies of National Polytechnic Institute, CINVESTAV-IPN, 07360, Mexico City, Mexico*

KEYWORDS: Organic solar cells, Lithium Fluoride and PFN, Fill factor, Low bandgap polymer, Diode model

Optimization of the LiF layer on the photovoltaic devices type I-X and type II-X

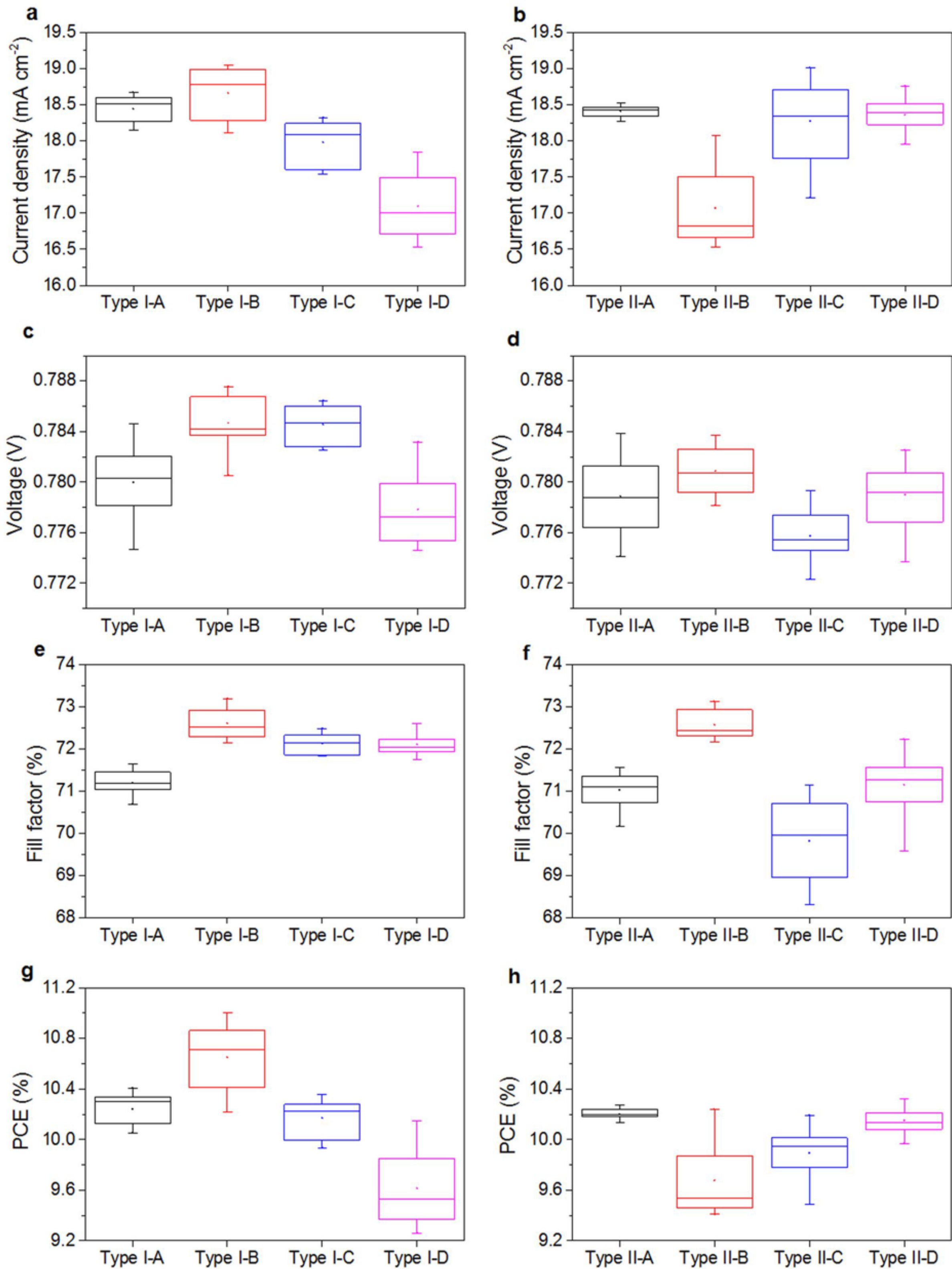

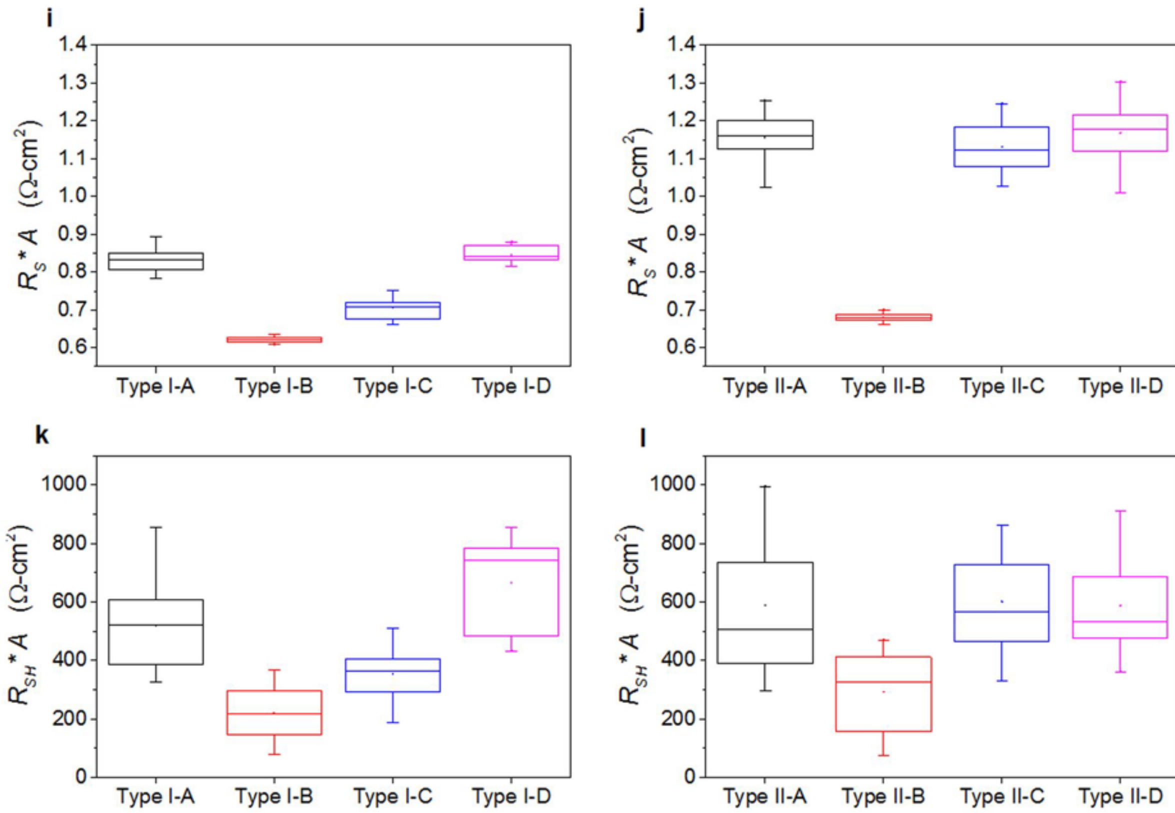

Fig. SI1. Device performance optimization. Performance parameters of i-OSCs for type I-X and type II-X structures are shown. The letter X means different LiF layer thickness: A, B, C and D represents 0.5 nm, 0.6 nm, 0.7 nm and 0.8 nm, respectively. The devices were measured at one sun under the simulated AM 1.5 spectrum (100 mW cm^{-2} irradiance). The data are represented as a standard box plot where the box range is defined by the s.d. (standard deviation). Performance data based according the structures: a) and b) are short circuit current density (J_{SC}), c) and d) are open circuit voltage (V_{OC}), e) and f) are fill factor (FF), g) and h) are power conversion efficiency (PCE), i) and j) are series resistance (R_S) and k) and l) are shunt resistance (R_{SH}).

Short circuit current, open circuit voltage and fill factor analysis

One of the most frequently asked questions regarding, how many is the maximum theoretical *Jsc* that can reaches and gives a semiconductor organic material to be used as photovoltaic device? The upper limit of theoretical value of short circuit current density (J_{TSC}) that can gives a semiconductor organic material can be calculated considering the next context: under ideal conditions, for each photon incident (under the AM 1.5 solar energy spectrum) on the material with energy greater than the band gap (E_g) which gives rise to generate one free electron flowing in the external circuit, it is possible calculate using **Equation 1**:[1]

$$J_{TSC} = q * \int_{\lambda_{min}}^{\lambda_{Eg}} N(\lambda) * \, d\lambda \qquad (1)$$

where q is the elementary charge, λ_{Eg} is band gap energy of the semiconductor material in wavelength, λ_{min} is the minimum wavelength that absorbed the material semiconductor, $N(\lambda)$ is the number of photons absorbed at a wavelength. The E_g for the active layer PBDTTT-EFT:$PC_{70}BM$

was obtained using Tauc's method as is showed in **Figure SI2** of supplementary information to be of 1.376 eV. Determining J_{TSC} by **Equation 1** gives a value of 28.77 mA cm^{-2}.

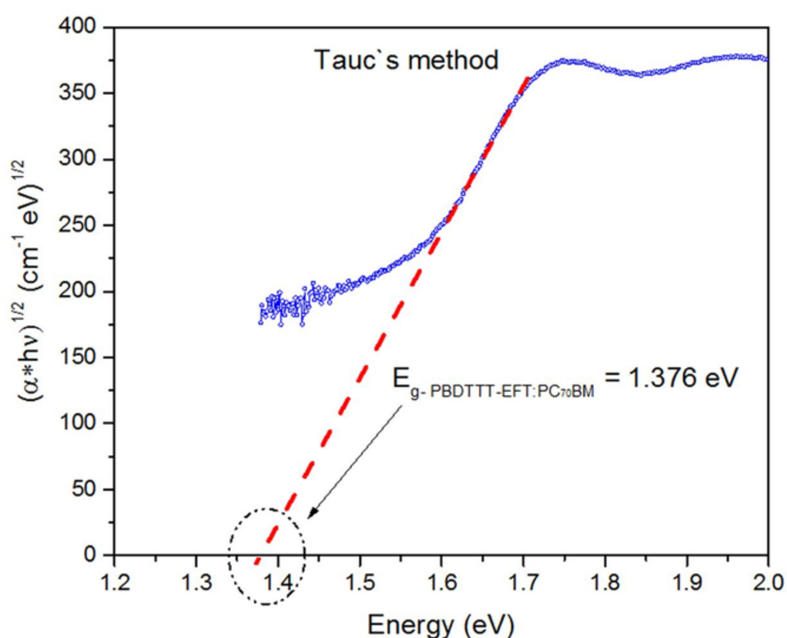

Fig. SI2. Determination of the band gap (***E_g***)**.** The Eg was determined by Tauc's method of the active layer PBDTTT-EFT:$PC_{70}BM$ used to quantify the probable maximum theoretical value of J_{SC} for all i-OSCs.

Therefore, the J_{SC} reached up until now represents ~ 66.2% regarding the maximum theoretical. While that ~ 33.8% could be considered as loss by parasitic resistances (i.e. contact resistance, active layer, and metallic contacts), recombination process at the interfaces of the layers, losses by increment of the reflectance inside of the structure, losses by absorbance, among many others. On the other hand, this suggests that there is the possibility to follow in the search of new materials as ETLs to be used in the structure and thus improve more the J_{SC} of the OSCs.

As first parameter with influence on the PCE of all the structures analyzed was the J_{SC} which this was explained in the manuscript. A second parameter with high influence on the PCE is the V_{OC}. **Fig. SI8b** and **Table 2** show the tendency of V_{OC} according the type ETLs used for each structure. The V_{OC} increment reached for type I-B, type II-B, type III and type IV structures regarding the type V structure (without ETL) were 13.4%, 12.82%, 13.11% and 10.95%, respectively. Some reports have shown that the cathode/acceptor interface plays a predominant role in determining V_{OC} in i-OSC of BHJ which this will be discussed in more detail belong.[2]

On the other hand, it has been observed that reverse saturation current density (J_0) shows a quantitative and qualitative relationship with V_{OC} in the solar cell.[3-5] To accurately extract J_0 values

from the *J–V* experimental curves of all structures photovoltaics has been modeled using an equivalent circuit as is shown in **Fig. SI3a.**

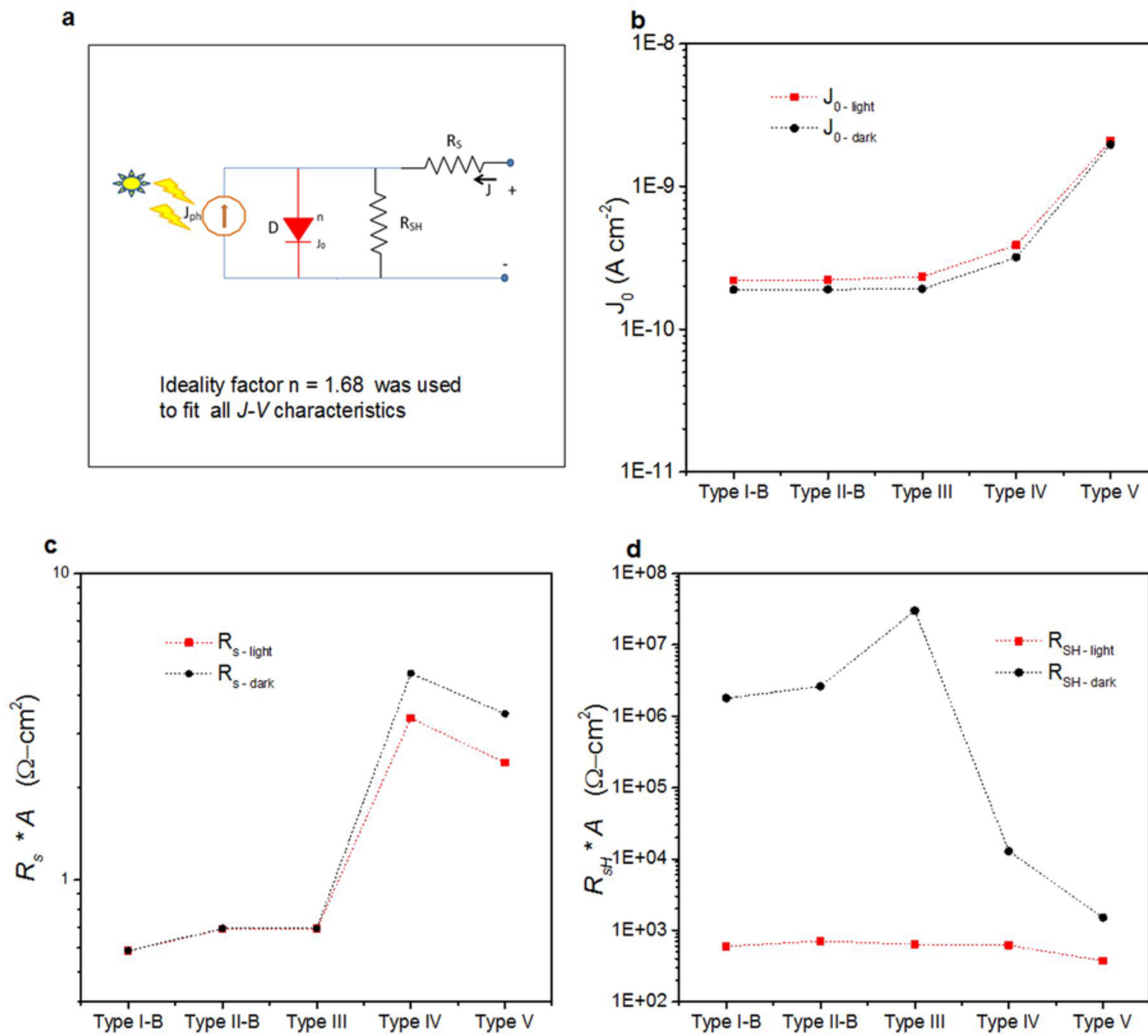

Fig. SI3. Modeling of the photovoltaic devices. a) Circuital model used to fit all the *J–V* characteristics under light and dark conditions for the five structures manufactured and analyzed in this work. b) Saturation current (J_0). c) Series resistance per unit area ($R_{S*}A$) and d), shunt resistance per unit area ($R_{SH*}A$) parameters were extracted from the **Equation 2**. The red and black dotted lines in the graphs are only to guide the eyes.

All i-OSCs analyzed in our work can be modeled using a single diode with the assumption that a specific conduction mechanism is predominant. The current density in the circuit is given by:[3, 6]

$$J = J_0\left[exp\left[\frac{q(V-JAR_s)}{nkT}\right]-1\right]+\frac{V-JAR_s}{R_{SH}A}-J_{ph} \qquad (2)$$

where V is the voltage applied, A is the active area of the device, *n* is the factor ideality, k is the Boltzmann constant, T is the temperature, J_{ph} is the photocurrent, R_S is the series resistance and R_{SH} is the shunt resistance. The J_0 was obtained by two methods. The first method to get J_0 was

from the intersection of the diode region with the current density axis from *J–V* curves under darkness as is shown in **Fig. 2b (see manuscript)**. The second method used to obtain J_0 was extracting the parameter from the fitted curve using the **Equation 2** against the *J–V* experimental data under darkness or light curves. The J_0 values obtained for each structure are depicted in **Fig. SI3b**. We have observed that the tendency of J_0 is intimate related with the cathode contact used as it is also reported by several authors.[4] The J_0 obtained under darkness for type I-B, type II-B, type III structures are around of 1.90 x 10^{-10} A cm^{-2} and the type IV and type V structures are ~ 3.19 x 10^{-10} A cm^{-2} and 1.96 x 10^{-9} A cm^{-2}, respectively. The J_0 of all the structures under illumination conditions were also extracted using the **Equation 2** and they are shown in **Fig. SI3b**. The J_0 increment under light for the first four structures were from 15% to 21%, and for the type V structure was 6% regarding the J_0 under darkness. It is well known that the meaning of J_0 in OSCs is associated with the number of charges capable of overcoming the energetic barrier in the reverse direction. It represents the minority charge density in the vicinity of the barrier.[7] At lowest values of J_0 the photovoltaic devices reach the highest efficiencies which this tendency was observed in our devices.

The ideality factor obtained by **Equation 2** for all the structures was 1.68. This parameter reflects the dominant charge transport and recombination mechanisms of the diode formed by the active layer. It has been observed that in high-efficiency solar cells the *n* is usually in the range 1.3–1.8, but can be larger in low-efficiency cells.[8] In our cells, according the *n* value obtained the charge transport mechanism can be due to a combination of diffusion with recombination mechanisms seems to be present.

From the J_0 and *n* values estimated above were used to predict the different V_{OC} of all the structures analyzed in this work. Firstly, we consider the equivalent circuit model for an ideal solar cell by assuming infinite R_{SH} and zero series resistance. Under V_{OC} conditions, the measured current is zero. Using these terms and applied to **Equation 2**, we obtain the following relation for the V_{OC}:[4, 8]

$$V_{OC} = \frac{nkT}{q} ln\left[\frac{J_{ph}(V_{OC})}{J_0} + 1\right] \approx \frac{nkT}{q} ln\left[\frac{J_{ph}(V_{OC})}{J_0}\right] \quad (3)$$

where $J_{ph}(V_{OC})$ is the photogenerated current density at $V=V_{OC}$, which is equal to the dark current density at V_{OC}. With **Equation 3** and the ideality factors where it is considering that all the photovoltaic structures have the same transport mechanism, therefore we can readily calculate the expected open circuit voltage for devices with the type I-B, type II-B, type III, type IV and type V structures give 0.793 V, 0.791 V, 0.789 V, 0.767 V and 0.695 V, respectively. It is worth noticing that there are good agreements obtained with the experimental (see **Table 2 in the manuscript**) and predicted values. **Fig. SI4** shows graphically the experimental and predicted values of V_{OC}.

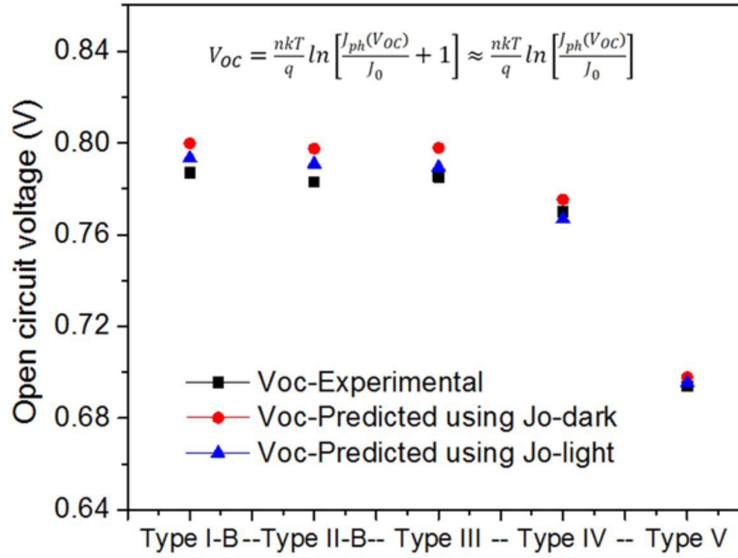

Fig. SI4. Modeling the V_{OC}. Experimental and predicted values of open circuit voltage were obtained for each group of i-OSCs manufactured. The V_{OC} predicted value has dependence with the saturation current density (J_0) which was extracted from **Equation 3**. (J_0) was taken and extracted of *J–V* curves under dark and light conditions.

It is observed that the increase in open circuit voltage is a direct outcome of the hole blocking effect of type electrons transport layer used with or without it. Several reports have attributed that the increase of the open circuit voltage is by the higher charge carrier densities and its high balanced distribution of charges where is reduce the internal electric field.[9, 10] In this case the charge carrier densities reached for these devices are ~1.77 x 10^{21} cm^{-3} as is reported elsewhere.[11] By first time is shown and reported the predicted values of V_{OC} for different i-OSCs where a combination of one organic interlayer (PFN) with haloid salt layer (LiF) were utilized as ETLs.

Studies concerned to fill factor is other parameter with influence on the PCEs of the photovoltaic devices. The solar cell fill factor is defined as:[12, 13]

$$FF = \frac{J_{max} * V_{max}}{J_{SC} * V_{OC}} \qquad (4)$$

where J_{max} and V_{max} are the current density and voltage, respectively, at the maximum power output of the solar cell. J_{max}, V_{max}, J_{SC} and V_{OC} are extracted from theirs *J–V* experimental curves. The FF is obtained using **Equation 4** for type I-B, type II-B, type III, type IV and type V structures giving 73.50%, 73.12%, 72.17%, 65.22% and 61.95%, respectively. Therefore, the best FF is for type I-B architecture having an increment of 18% regarding the type V architecture (without ETL). In the last three decades expression for evaluating solar cell fill factors applied to different technologies have been reported as simple empirical and complex expression.[14-18] From *J–V* curves,

the FF can be understood as the degree of how rectangular *J–V* characteristic exhibits the photovoltaic device. From other point of view, the FF can be regarded as how easily photo-generate carriers could be swept out under the field resulting from the build-in potential and external applied bias. To get a maximum FF on the photovoltaic devices is necessary that the built-in potential decreased when is applying external applied bias. The expressions to calculate and predict the solar cell FF derives a simple but accurate empirical expression which considers parasitic resistances such as series and shunt (FF_{RS+RSH}) being frequently the real case for OPVs. A simplified and approximated expressions for the $FF_{R_S+R_{SH}}$ are shown as follows:[16, 18]

$$FF_{R_S+R_{SH}} = FF_{R_S} * \left[1 - \frac{v_{oc}+0.7}{v_{oc}} * \frac{FF_{R_S}}{r_{SH}}\right] \quad (5)$$

$$FF_{R_S} = FF_0 * [1 - r_S] \quad (6)$$

$$FF_0 = \frac{v_{OC} - ln\,[v_{OC} + 0.72]}{v_{OC} + 1} \quad (7)$$

$$r_{SH} = R_{SH} * \frac{J_{SC}}{V_{OC}} \quad (8)$$

$$r_S = R_S * \frac{J_{SC}}{V_{OC}} \quad (9)$$

$$v_{OC} = \frac{q*V_{OC}}{nkT} \quad (10)$$

where the FF_{R_S} is the fill factor only influenced by series resistances, FF_0 is the fill factor without influence of parasitic resistances, r_{SH} is the normalized shunt resistance, r_S is the normalized series resistance, v_{OC} is the normalized open circuit voltage. Using the **Equation 5** and **Equation 6** accuracy with one digit in the second significant place can be reached. Likewise, **Equation 7** the accuracy of this expression approaches to one digit in the fourth significant place when the value of normalized open circuit voltages is larger than 10.[16]

To estimate the $FF_{R_S+R_{SH}}$, first of all is necessary to get R_S and R_{SH} values which these were calculate by two different ways.

The first method to obtain R_S and R_{SH} were calculated by the inversed slope of the *J–V* curve at the highest operating voltage where the curve becomes linear: $R_S=(J/V)^{-1}$, and the inverse slope around 0 V of the *J–V* curve, $R_{SH}=(J/V)^{-1}$, respectively, as was reported elsewhere.[19, 20] **Fig. SI5a** shown three linear regions of Log J-V curves under darkness when the devices are bias forward. After, all the cell groups are analyzed. On experimental J-V graphs were extracted series resistances using the first method describe above. Open symbols represent experimental data and continuous line means the modeled curves. Fig. SI5b shows an approach of region III.

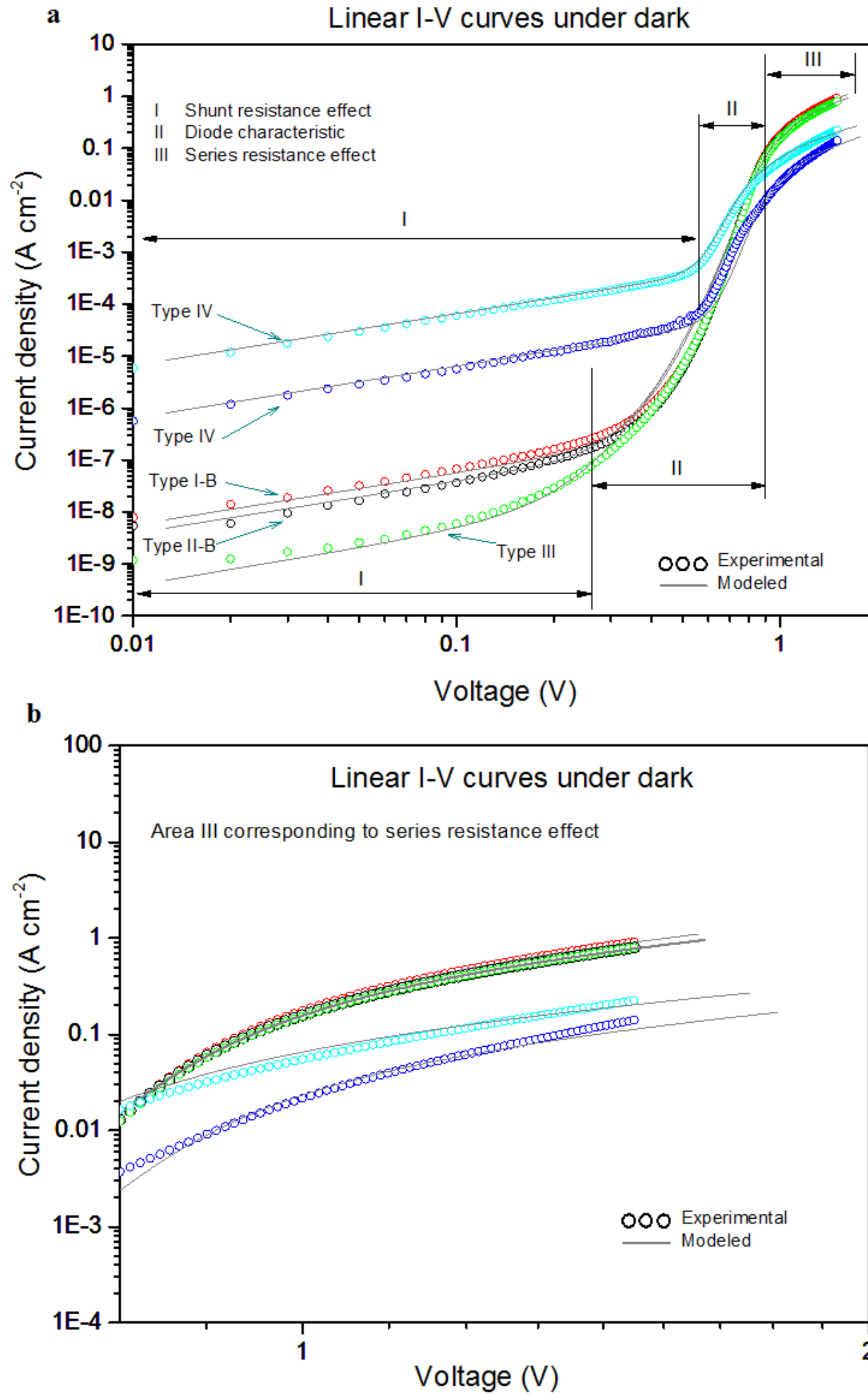

Fig. SI5. Log J-V curves under darkness. a) Three regions identifyed which the first one corresponds to shunt resistance effect; second one is related to the diode characteristic; third one corresponds to series resistance effect. b) Approach of region III.

Second method to obtain R_S and R_{SH} were obtained from the measurement *J–V* characteristic modeled by the **Equation 2.** Both resistances values were obtained under illumination and darkness conditions. Using the first method, R_S and R_{SH} values are summarized in **Table 1** (see manuscript)

and **Table 2** (see manuscript). On the other hand, using the second method the R_S and R_{SH} values can be observed in **Fig. SI3c** and **d**, respectively.

Predicted R_S and R_{SH} have a good agreement regarding the experimental values and these will be analyzed below.

Obtained the R_S and R_{SH}, the FF=$FF_{R_S+R_{SH}}$ for type I-B, type II-B, type III, type IV and type V structures were calculated by using **Equation 5** being of 73.85%, 74.17%, 73.82%, 66.75% and 62.63%, respectively. We note a good agreement between the experimental and predicted values. We have demonstrated that the FF in our i-OSCs depends on the R_S and R_{SH} values and mainly of type ETL used. All the experimental values were predicted satisfactorily by using **Equation 5**. In **Fig. SI6** displays the graph of experimental and predicted values of FF. **Table SI1** summarizes the respective values of FF_{R_S}, FF_0, r_{SH}, r_S and v_{OC} used to get FF.

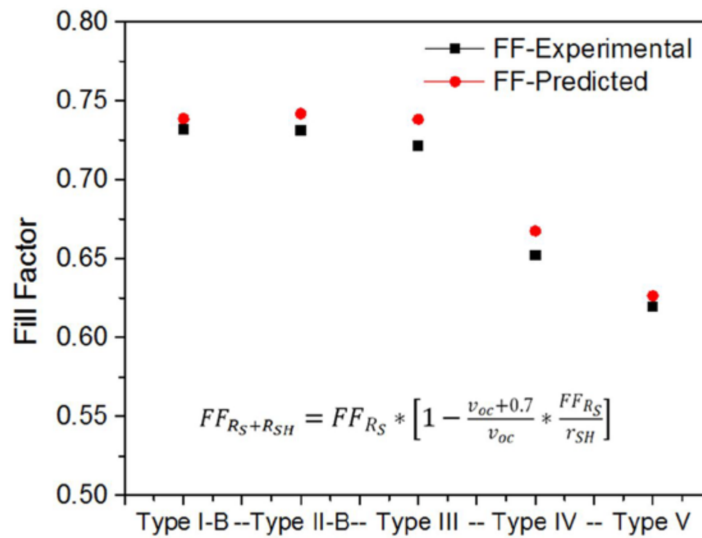

Fig. SI6. Fill factor modeling. Experimental and predicted values of fill factor obtained for each group of i-OSCs manufactured. The FF predicted value has dependence with the series and shunt resistances which was extracted from **Equation 5**.

Table SI1. Parameters used to predict the FF for all devices structures manufactured.

Device Description	FF_{RS}	FF_0	r_{SH}*	r_S*	Voc*
Type I -B	0.78298	0.79421	14.33443	0.01415	18.12896
Type II-B	0.78078	0.79348	16.24229	0.01600	18.03681
Type III	0.78095	0.79385	14.82210	0.01624	18.08289
Type IV	0.70278	0.79103	14.55381	0.11157	17.73735
Type V	0.70211	0.77536	6.79229	0.09448	15.98665

In general, the performance parameters of the inverted and standard structures reported in literature with our results is summarizes in **Table SI2**. The active layer used to compare with the different solar cells is PBDTTT-EFT:$PC_{70}BM$. It is worth noting that our i–OSC is one of the first to be manufactured with one organic interlayer (PFN) deposited on haloid salt layer (LiF) as ETL, about which no reports have been published to date. The PCE obtained here of 11.00% of one junction which is comparable with such other standard ETLs is higher than all others report in the literature. Finally, we have found that V_{OC} is dependent of J_0 and as well they have dependence of the equivalent work function according the type stack selected. We have plotted these parameters, x, y and z axes represent J_0, Φ_{Effect} and V_{OC} values, respectively for each structure analyzed. Uniting all the points was generated a surface which the plot gives the general tendency of these data as can see in **Fig. SI7**.

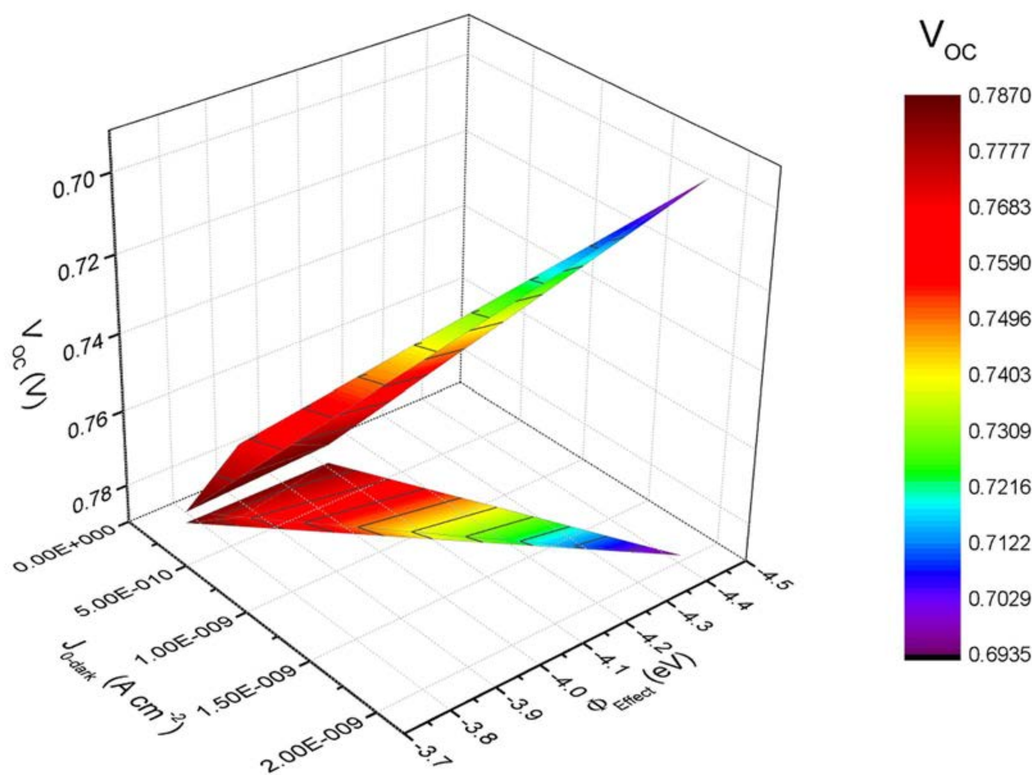

Fig. SI7. Correlation of parameters. Plot shows the correlation of the saturation current density (J_0) and open circuit voltage (V_{OC}) dependent of effective work function (Φ_{Effect}).

Table SI2. Performance summary of the photovoltaic devices reported in the literature. The PBDTTT-EFT:$PC_{70}BM$ is used as active blend layer.

	Device structure	Type	J_{SC} [a] [mA cm^{-2}]	V_{OC} [b] [mV]	FF [c] [%]	PCE [d] [%]	Rs*A [e] Ω-cm^{-2}	Rsh*A [f] kΩ-cm^{-2}	Ref.
A	ITO/HAPAN/PBDTTT-EFT:$PC_{70}BM$/Ca/ Ag	Std	16.51	789	69.50	9.05	7.96	0.890	21
B	ITO/PEDOT:PSS/PBDTTT-EFT:$PC_{70}BM$/LiF/ Al	Std	14.88	790	64.50	7.58	2.50	0.116	22
C	ITO/PEDOT:PSS/PBDTTT-EFT:$PC_{70}BM$/Ca/ Al	Std	16.86	784	68.16	9.00	---	---	23
D	ITO/PEDOT:PSS/PBDTTT-EFT:$PC_{70}BM$/ Al	Std	19.80	790	65.00	10.12	2.00	1.500	24
E	ITO/PEDOT:PSS/ PBDTTT-EFT:$PC_{70}BM$/C_{60}/ Al	Std	19.01	820	69.10	10.80	---	---	25
F	ITO/PEDOT:PSS/PBDTTT-EFT:$PC_{70}BM$/LiF/ Al	Std	17.11	800	55.20	7.60	---	---	26
G	ITO/PEIE/PBDTTT-EFT:$PC_{70}BM$/MoO_3/ Ag	Inv	18.10	790	66.00	9.50	---	---	27
H	ITO/TiOx/PBDTTT-EFT:$PC_{70}BM$/MoO_3/ Ag	Inv	15.10	790	50.00	6.00	---	---	28
I	ITO/PFN/PBDTTT-EFT:$PC_{70}BM$/MoO_3/ Al	Inv	17.43	825	73.78	10.61	---	---	29
J	ITO/PEIE/PBDTTT-EFT:$PC_{70}BM$/MoO_3/ Ag	Inv	18.3	790	62.00	9.00	---	---	30
K	ITO/ZnO/ $PF_{EO}SO_3Na$/PBDTTT-EFT:$PC_{70}BM$/MoO_3/ Al	Inv	17.79	780	67.80	9.41	---	---	31
L	ITO/patterned ZnO/PBDTTT-EFT:$PC_{70}BM$/MoO_x/ Al	Inv	19.47	780	66.90	10.10	---	---	32
M	ITO/AZO/PBDTTT-EFT:$PC_{70}BM$/MoO_x/ Ag	Inv	17.70	800	70.70	9.94	---	---	33
N	ITO/ZnO:PBI-H/PBDTTT-EFT:$PC_{70}BM$/MoO_3/ Al	Inv	17.69	820	72.90	10.59	---	---	34
O	ITO/ZnO-C_{60}/PBDTTT-EFT:$PC_{70}BM$/MoO_3/ Ag	Inv	15.73	800	74.30	9.35	---	---	35
P	ITO/ZnO/PBDTTT-EFT:$PC_{70}BM$/MoO_3/ Ag	Inv	19.30	810	70.00	10.95	---	---	36
[Q]	ITO/PFN/LiF/PBDTTT-EFT:$PC_{70}BM$/V_2O_5/ Ag	Inv	19.05	787	73.50	11.00	0.63	0.366	

[a] Open circuit voltage. [b] Short circuit current. [c] Fill factor. [d] Power conversion efficiency. [e] Series resistances per unit area. [f] Shunt resistances per unit area. The illumination intensity equivalent applied was at 100 mW cm^{-2} after the spectral mismatch correction using an AM 1.5G solar simulator. [Q] Result from this contribution. Std means standard structure. Inv means inverted structure.

Series and shunt resistances

In general, the parasitic resistances calculated above have influence on the PCE. The series resistances is well known that can be related to the resistance and thickness of the active layer, the contact resistance between the metal or ETL with active layers, the transport properties of the semiconductor material and the type of the selective contacts used for the devices.[7, 12] **Fig. SI8e** illustrates the statistical values of R_S for each group of cells manufactured.

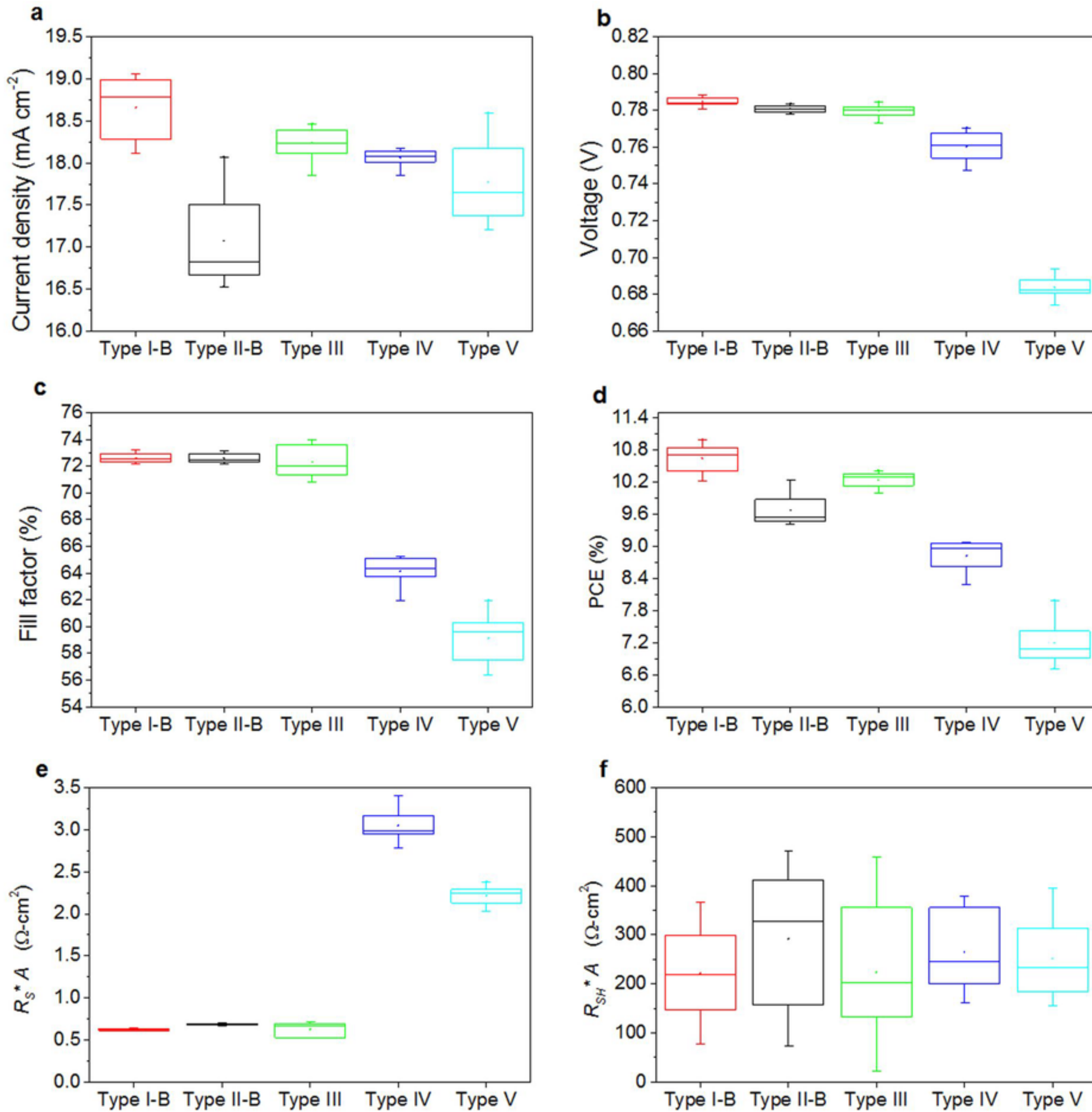

Fig. SI8. Performance parameter of the structures. Performance parameters of inverted organic solar cells are shown for all the different architectures which were analyzed and compared (type I-B, type II-B, type III, type IV and type V). The LiF layer thickness was 0.6 nm. The devices were measured under simulated AM 1.5 spectrum sunlight (100 mW cm^{-2} irradiance). The data are represented as a standard box plot where the box range is defined by the s.d. (standard deviation). Performance data based according the structures: a) is J_{SC}, b) is V_{OC}, c) is FF, d) is PCE, e) is $R_{S*}A$ and f) is $R_{SH*}A$.

While that in **Table 2** (see manuscript) shows the series resistances values per unit area under light and darkness conditions $R_{S-light}*A$ and $R_{S-dark}*A$, respectively which these were extracted from *J*–*V* curves using the first method. R_S and (aver.) values under light conditions for type I-B, type II-B, type III, type IV and type V structures were 0.63 Ω-cm^2 (aver. 0.62 Ω-cm^2), 0.70 Ω-cm^2 (aver. 0.68 Ω-cm^2), 0.71 Ω-cm^2 (aver. 0.63 Ω-cm^2), 3.39 Ω-cm^2 (aver. 3.04 Ω-cm^2), and 2.37 Ω-cm^2 (aver. 2.21 Ω-cm^2), respectively. The type I-B architecture presented the lowest R_S. On the other hand, the

type IV architecture was 5.4 time bigger the R_S regarding type I-B structure. In fact, these differences of resistances are attributed to the differences ETLs used. We have observed that the R_S has influence on the FF.[12, 16] This parameter is completely asserted with **Equation 5** where the FF is dependent of R_S. The higher the series resistances, the lower FF will be. In our devices this tendency is observed except for the type IV structure. This effect can be explained and attributed due to lack of LiF layer uniformity (0.6 nm of thickness) on the ITO layer. It is well known that when the LiF layer is deposited with extremely thin thickness, partial LiF molecules are distributed randomly as clusters or island on the ITO or even this has the same behavior when is also deposited on organic layers.[6, 37, 38]These islands indicate that the ITO was not fully covered with LiF when an extremely thin layer of LiF was evaporated on the surface of the ITO. These islands are detrimental to the performance of the OPVs. The regions of ITO that not were covered partially with LiF act as short pathways, resulting in decreases in the shunt resistance. In addition to decreasing the R_{SH}, these islands cause high values of the surface roughness, which lead to increases in the R_S due to the increases in contact resistance between the ITO and the active layer and also resulting a high surface recombination of charges carriers between of them as is observed in **Fig. 5h** (see manuscript). Therefore, this phenomenon is identical in ours devices with the type IV structure regarding other reports. [6, 37, 38]

Eventually following with the analysis of R_S, the reduction of 10% was for type I-B (stack ITO/PFN/LiF) regarding the type II-B (stack ITO/LiF/PFN) structures. This decrement in R_S is due to that the ITO surface was covered totally by PFN layer when was deposited by spin-coating method, thus that there are not losses by leakage current or formation of short pathways. But immediately a question arises, what does happen when is deposited the LiF layer on the PFN surface? The answer for this question is that on the PFN surface layer are generated islands of LiF as was explained above. These LiF islands lead to unintentional doping at the interface of PFN with the active layer which could be named as “charged interfaces” as it is the same case for other materials.[39-41] This term is generally used when charged interfaces is given at the donor-acceptor interface of the active layer.[40] With this fixed charge layer creates a local electric field at the interface, which prevents the carrier pileup and thereby reduces the interfacial recombination dramatically, which would in turn significantly improves the FF and decrease the R_S. From other point of view, the morphology of this configuration (ITO/PFN/LiF) becomes more smooth as was observed in **Fig. 5e** (see manuscript). This effect could be partially the same at interface of PFN with active layer of our devices where finally the PCE is improved. The embedded materials reported to generate the charged interfaces can be as the haloid salt (i.e. LiF, fluorinate compound, etc).[42, 43] It is knows from the literature that the surface contact of ITO with PFN or ITO with LiF

can set up to lead an interfacial dipole moment.[44-46] Therefore, we could be suggested likely that the interface between PFN with LiF can or not leads an increase of interfacial dipole moment.

Meanwhile for the type II-B structure the slight increase of R_S is attributing to the resulting combination of two surface interfaces manufactured: firstly, the not surface homogeneity of ITO with LiF layer identically as the stack of type IV structure; secondly, the good surface homogeneity deposited of PFN layer on the thin LiF layer. The first interface layer creates the problem of increment of R_S while that the second deposition corrects the problem of interface which finally decreased the R_S of stack as is observed in **Fig. 5g** (see manuscript).

Theoretical estimates when $R_S \approx 0$ (in this case for the type I-B structure), the maximum PCE, FF and Voc that might be reached regarding the experimental values would be of 11.23%, 74.9% and 0.790 V, respectively. These predicted performance parameters were estimated by using **Equation 2** as can be seen in **Fig. SI9**. J_{SC} remain without variation when is used **Equation 2**.

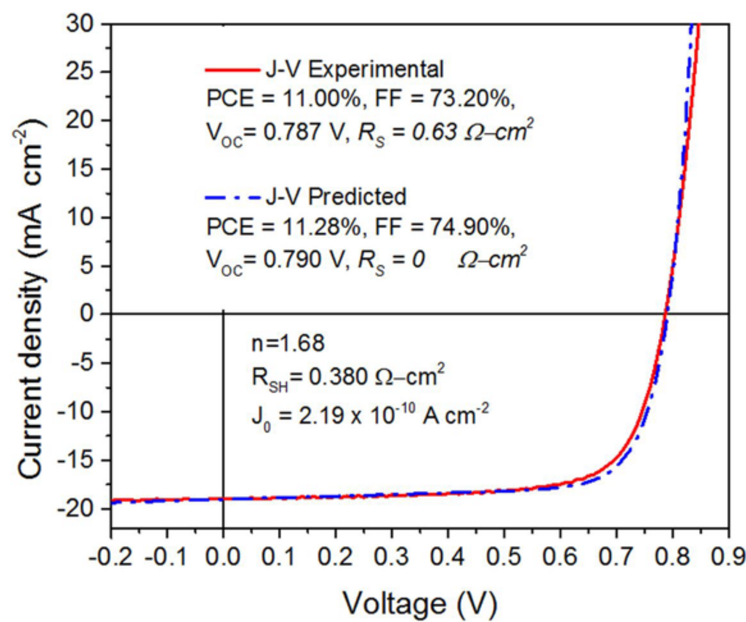

Fig. SI9. J-V predicted. Experimental and predicted *J–V* characteristics under illumination of type I-B group of i-OSCs. The *J–V* curve predicted was modelled using **Equation 2**. J_0, *n* and R_{SH} were the same parameters to model the *J–V* curves.

On the other hand, the shunt resistance R_{SH} is related to the recombination of charge carriers near the dissociation site (i.e. the donor/acceptor interface of the bulk heterojunction) and also depends on the transport properties of the semiconductor.[7] **Fig. SI8f** illustrates the statistical values of $R_{SH*}A$ obtained for type I-B, type II-B, type III, type IV and type V structures. **Table 2** (see manuscript) summarized the shunt resistance values per unit area for each group under light and dark conditions $R_{SH-light}*A$ and $R_{SH-dark}*A$, respectively which were obtained using the first method and in **Fig.**

SI3d are displayed the values applying the second method (i.e. using **Equation 2**). It is well known that when the cell is not illuminated, this parallel shunt resistance is expected to reflect the intrinsic conductivity of the materials. Under illumination, light induced charge generation (photodoping) caused by the charge transfer between the donor and the acceptor is expected to reduce the shunt resistance dramatically, as was clearly observed in our results.[19, 20] In general, $R_{SH} * A$ values under light conditions for all structures are in the order 10^2 Ω-cm^2. The lower the shunt resistance under darkness, the higher charge carrier recombination process at donor/acceptor interface of the bulk heterojunction will be. **Fig. SI3d** displays that the type V structure presented the lower $R_{SH} * A$ of all the architectures of 1.68 x10^3 Ω-cm^2. This is attributed due to that the architecture is without ETL, therefore the increase of the leakage current is very higher. On the other hand, type I-B and type II-B structures are in the order 10^6 Ω-cm^2. Finally, type III structures presented the higher R_{SH} values and are in the order 10^7 Ω-cm^2.

Photoinduced techniques for charge collection and carrier recombination analysis

Photoinduced transient techniques have been employed to investigate the interfacial carrier recombination dynamics in complete devices, including organic solar cells and recently in perovskite cells. Setup details and an extensive explanation of the techniques is reported elsewhere.[47] Among them, charge extraction (CE) has been proved to be a consistent method to estimate the charge density in different types of solar cells. The device under testing is held at open circuit conditions during the illumination and, once steady state is reached, the light is switched off and simultaneously the device is short-circuited allowing it to discharge. CE measurements were conducted as a function of light intensity and thus voltage (photoinduced V_{OC}).

The structures of type ITO/PFN, ITO/LiF/PFN and ITO/PFN/LiF have been measured and the results are depicted in **Fig. SI10a**. All devices present similar trend indicating that, in this case, the contact configuration does not affect charge accumulation.

In order to estimate the recombination processes in the device under working conditions, the transient photovoltage (TPV) measurement has been used. A continuous light bias is applied to the device and a laser pulse (at a wavelength where the IPCE of the device is sufficiently high) generates an additional amount of charges, which cannot be extracted as the device is held in open circuit so they are forced to recombine. In open circuit condition, the net current flowing through the device is zero implying that any effect arising from the series resistance is not affecting the measurement. The result is an exponential decay (see **Fig. SI10b**) in which the time constant (small perturbation lifetime) is associated with the interfacial carrier recombination.

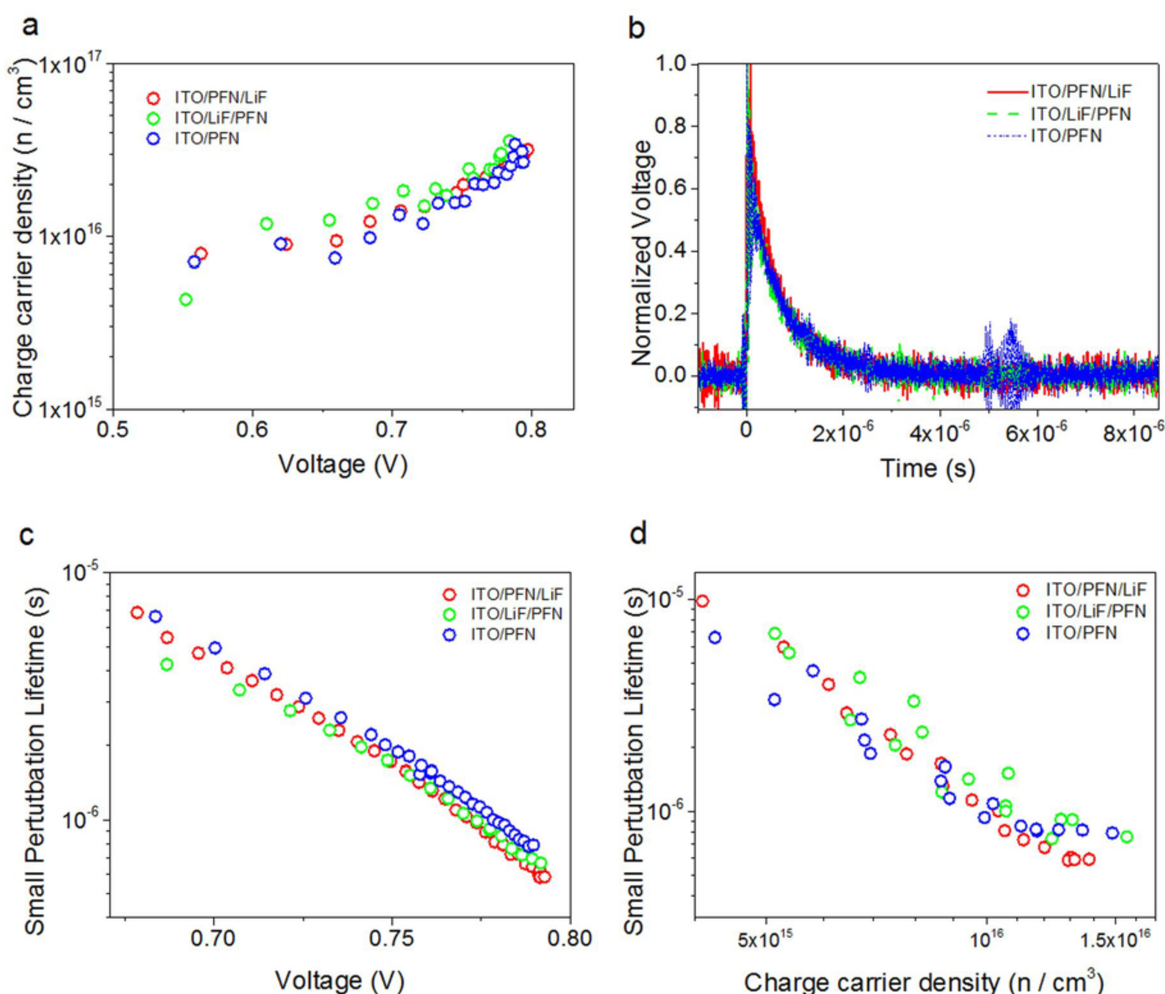

Fig. SI10. Charge extraction and transient photovoltge measurements.

TPV measurements, also taken at different light intensities and thus V_{OC} (**Fig. SI10c**), give comparable results with recombination lifetime at 1 Sun equivalent illumination between 0.6 and 0.8 μs (**Fig. SI10b**). The excitation wavelength was 500 nm.

In **Fig. SI10d** it is possible to compare carrier recombination lifetimes between different devices at the same charge density combining the results of CE and TPV: recombination lifetimes are almost equal for the three configurations at a given charge density, confirming that contact configuration does not directly affect the recombination.[48]

***J-V* measurements taken in forward and reverse bias**

The J-V measurements have been taken in forward and reverse voltage in order to know if the hysteresis is presented in the devices. **Fig. SI11a** shows the structure Type I-B where the no hysteresis has been observed for the organic solar cells.

Photocurrent at maximum power point has been checked under short period of time under 1 Sun illumination (100 mW cm^{-2}) condition to calculate the PCE which the MPP was 0.65V as is shown in **Fig. SI11b**.

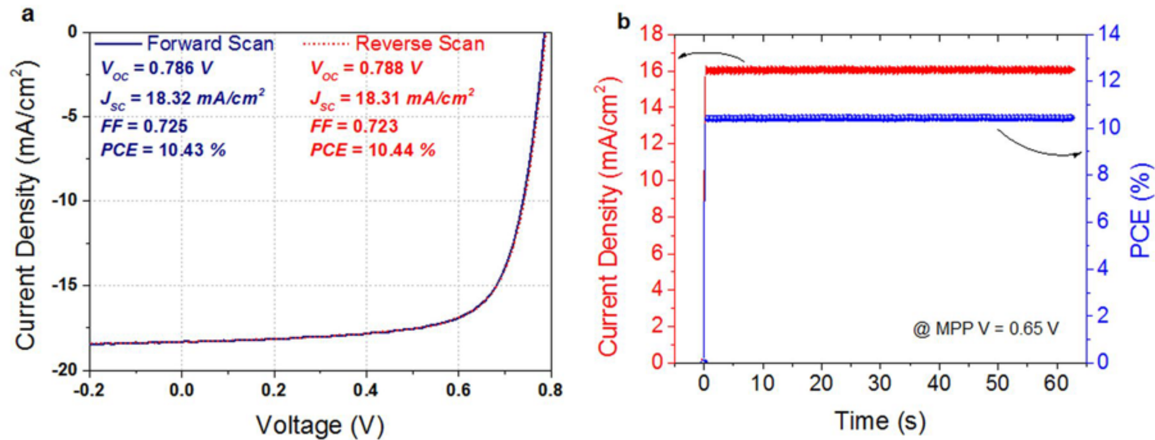

Fig. SI11. Current-Voltage in forward and reverse bias and the phtotocurrent at maximum power point at 1 sun.

Acknowledgements

The work of Victor S. Balderrama (ID Researcher 7340 and CVU-227699) was supported by "Cátedra-CONACYT para Jóvenes Investigadores" under the Call 2017 from the Project Number 2 "Strengthening Scientific Capacity and Human Capital for the Development of MEMS for the Industry" in Querétaro, Mexico and Project Number 293384, "Laboratorio Nacional SEDEAM CONACYT" under the Call 2018 "Apoyos Complementarios para la Consolidación de Laboratorios Nacionales CONACYT". This work was supported by the Consejo Nacional de Ciencia y Tecnología (CONACYT) under the Project 237213 in Mexico. We give thanks to National Postdoctoral Fellowship from CONACYT under the Call 2017-2 and adjudge to Gonzalo Lastra (CVU-223920). We give thanks to the Spanish Ministry of Economy and Competitiveness (MINECO-FEDER TEC2015-71324-R) and TEC2015-71915-REDT in part by the Catalan Government 2017-SGR-1527, the ICREA under the ICREA Academia Award.

Bibliography

1. G. Dennler, M. C. Scharber and C. J. Brabec, *Adv. Mater.*, 2009, **21**, 1323-1338.
2. V. D. Mihailetchi, P. W. M. Blom, J. C. Hummelen and M. T. Rispens, *J. Appl. Phys.*, 2003, **94**, 6849-6854.
3. J. H. Lee, S. Cho, A. Roy, H.-T. Jung and A. J. Heeger, *Appl. Phys. Lett.*, 2010, **96**, 163303.
4. J. C. Nolasco, G. Ramos-Ortiz, J. L. Maldonado, O. Barbosa-Garcia, B. Ecker and E. v. Hauff, *Appl. Phys. Lett.*, 2014, **104**, 043308.
5. Y. Peng, L. Zhang and T. L. Andrew, *Appl. Phys. Lett.*, 2014, **105**, 083304.
6. G. M. Kim, I. S. Oh, A. N. Lee and S. Y. Oh, *J. Mater. Chem. A*, 2014, **2**, 10131-10136.
7. V. S. Balderrama, F. Ávila-Herrera, J. G. Sánchez, J. Pallarès, O. Vigil-Galán, L. F. Marsal and M. Estrada, *IEEE Journal of Photovoltaics*, 2016, **6**, 491-497.

8. R. A. Street, *Adv. Mater.*, 2016, **28**, 3814-3830.
9. J. Schafferhans, A. Baumann, A. Wagenpfahl, C. Deibel and V. Dyakonov, *Org. Electron.*, 2010, **11**, 1693−1700.
10. D. Cheyns, J. Poortmans, P. Heremans, C. Deibel, S. Verlaak, B. P. Rand and J. Genoe, *Phys. Rev. B*, 2008, **77**, 165332.
11. G. Lastra, V. S. Balderrama, L. Reséndiz, J. Pallarès, S. I. Garduño, V. Cabrera, L. F. Marsal and M. Estrada, *Submitted* 2017.
12. J. D. Servaites, S. Yeganeh, T. J. Marks and M. A. Ratner, *Adv. Funct. Mater.*, 2010, **20**, 97-104.
13. B. Qi and J. Wang, *Phys. Chem. Chem. Phys.*, 2013, **15**, 8972-8982.
14. M. A. Green, *Sol. Cells*, 1982, **7**, 337-340.
15. E. Sánchez and G. L. Araújo, *Sol. Cells*, 1987, **20**, 1-11.
16. M. A. Green, *Solid State Electron.*, 1981, **24**, 788-789.
17. M.-H. Jao, H.-C. Liao and W.-F. Su, *J. Mater. Chem. A*, 2016, **4**, 5784-5801.
18. M. A. Green, *Appl. Phys. Lett.*, 2016, **108**, 081111.
19. V. S. Balderrama, M. Estrada, P. L. Han, P. Granero, J. Pallarés, J. Ferré-Borrull and L. F. Marsal, *Solar Energy Materials and Solar Cells*, 2014, **125**, 155-163.
20. C. Waldauf, M. C. Scharber, P. Schilinsky, J. A. Hauch and C. J. Brabec, *J. Appl. Phys.*, 2006, **99**, 104503.
21. W. Zhao, L. Ye, S. Zhang, B. Fan, M. Sun and J. Hou, *Sci. Rep.*, 2014, **4**, 6570.
22. D. Wang, F. Zhang, L. Li, J. Yu, J. Wang, Q. An and W. Tang, *RSC Advances*, 2014, **4**, 48724-48733.
23. S. Zhang, L. Ye, W. Zhao, D. Liu, H. Yao and J. Hou, *Macromolecules*, 2014, **47**, 4653-4659.
24. One-Material, *Information obtained from One-Material: http://www.1-material.com/wp-content/uploads/2013/12/1M_From-PTB7-to-PCE-10_Confidential.pdf*, **2013**.
25. Q. Wan, X. Guo, Z. Wang, W. Li, B. Guo, W. Ma, M. Zhang and Y. Li, *Adv. Funct. Mater.*, 2016, **26**, 6635-6640.
26. H. Yan, J. G. Manion, M. Yuan, F. P. García de Arquer, G. R. McKeown, S. Beaupré, M. Leclerc, E. H. Sargent and D. S. Seferos, *Advanced Materials*, 2016, **28**, 6491-6496.
27. W. Huang, E. Gann, L. Thomsen, C. Dong, Y.-B. Cheng and C. R. McNeill, *Advanced Energy Materials*, 2015, **5**, 1401259-n/a.
28. A. J. Pearson, P. E. Hopkinson, E. Couderc, K. Domanski, M. Abdi-Jalebi and N. C. Greenham, *Org. Electron.*, 2016, **30**, 225-236.
29. Z. He, B. Xiao, F. Liu, H. Wu, Y. Yang, S. Xiao, C. Wang, T. P. Russell and Y. Cao, *Nat Photon*, 2015, **9**, 174-179.
30. W. Huang, E. Gann, Z.-Q. Xu, L. Thomsen, Y.-B. Cheng and C. R. McNeill, *J. Mater. Chem. A*, 2015, **3**, 16313-16319.
31. T. Yuan, X. Zhu, L. Zhou, J. Zhang and G. Tu, *Applied Physics Letters*, 2015, **106**, 083302.
32. J.-D. Chen, C. Cui, Y.-Q. Li, L. Zhou, Q.-D. Ou, C. Li, Y. Li and J.-X. Tang, *Advanced Materials*, 2015, **27**, 1035-1041.
33. L. K. Jagadamma, M. Al-Senani, A. El-Labban, I. Gereige, G. O. Ngongang Ndjawa, J. C. D. Faria, T. Kim, K. Zhao, F. Cruciani, D. H. Anjum, M. A. McLachlan, P. M. Beaujuge and A. Amassian, *Advanced Energy Materials*, 2015, **5**, n/a-n/a.
34. L. Nian, W. Zhang, N. Zhu, L. Liu, Z. Xie, H. Wu, F. Würthner and Y. Ma, *J. Am. Chem. Soc.*, 2015, **137**, 6995-6998.
35. S.-H. Liao, H.-J. Jhuo, Y.-S. Cheng and S.-A. Chen, *Advanced Materials*, 2013, **25**, 4766-4771.
36. J. Huang, J. H. Carpenter, C.-Z. Li, J.-S. Yu, H. Ade and A. K. Y. Jen, *Adv. Mater.*, 2016, **28**, 967-974.
37. Y. J. Lee, X. Li, D.-Y. Kang, S.-S. Park, J. Kim, J.-W. Choi and H. Kim, *Ultramicroscopy*, 2008, **108**, 1315-1318.
38. H. S. Kim, H. Lee, P. E. Jeon, K. Jeong, J. H. Lee and Y. Yi, *J. Appl. Phys.*, 2010, **108**, 053701.
39. S. Torabi, J. Liu, P. Gordiichuk, A. Herrmann, L. Qiu, F. Jahani, J. C. Hummelen and L. J. A. Koster, *ACS Appl. Mater. Interfaces*, 2016, **8**, 22623-22628.

40. B. Ray and M. A. Alam, 2012.
41. Z. Lu, X. Chen, J. Zhou, Z. Jiang, S. Huang, F. Zhu, X. Piao and Z. Sun, *Organic Electronics*, 2015, **17**, 364-370.
42. B. Yang, Y. Yuan, P. Sharma, S. Poddar, R. Korlacki, S. Ducharme, A. Gruverman, R. Saraf and J. Huang, *Adv. Mater.*, 2012, **24**, 1455-1460.
43. A. Tada, Y. Geng, Q. Wei, K. Hashimoto and K. Tajima, *Nat. Mater.*, 2011, **10**, 450-455.
44. Y. Gao, *Materials Science and Engineering: R: Reports*, 2010, **68**, 39-87.
45. J. M. Zhao, S. T. Zhang, X. J. Wang, Y. Q. Zhan, X. Z. Wang, G. Y. Zhong, Z. J. Wang, X. M. Ding, W. Huang and X. Y. Hou, *Appl. Phys. Lett.*, 2004, **84**, 2913-2915.
46. Z. He, C. Zhong, S. Su, M. Xu, H. Wu and Y. Cao, *Nat Photon*, 2012, **6**, 591-595.
47. J. W. Ryan and E. Palomares, *Adv. Energy Mater.*, 2017, **7**, 1601509-n/a.
48. A. Guerrero, N. F. Montcada, J. Ajuria, I. Etxebarria, R. Pacios, G. Garcia-Belmonte and E. Palomares, *J. Mater. Chem. A*, 2013, **1**, 12345-12354.